**PAPER** • **OPEN ACCESS**

# On the unsteady behaviours of the adiabatic endwall film cooling effectiveness

To cite this article: M Qenawy *et al* 2021 *IOP Conf. Ser.: Mater. Sci. Eng.* **1172** 012031

View the article online for updates and enhancements.


This content was downloaded from IP address 195.43.0.86 on 04/10/2021 at 10:05

# On the unsteady behaviours of the adiabatic endwall film cooling effectiveness

**M Qenawy [1], Y Liu [2] and W Zhou [2]**

[1] Faculty of Energy Engineering, Aswan University, Aswan 81528, Egypt.
[2] School of Mechanical Engineering, Shanghai Jiao Tong University, Shanghai 200240, China.

E-mail: m_qenawy@aswu.edu.eg.

**Abstract.** The film cooling technique is introduced in modern gas turbines to protect the blade from the high temperature of the incoming hot gases by forming a thin coolant blank over the blade surface. However, it is known as a jet in crossflow (JICF), where coolant and mainstream interact intensively and generate complex vortices leading to highly unsteady coolant coverage over the blades surface. In this study, a fast-response pressure-sensitive paint technique (fast-PSP) was used to measure the coolant unsteadiness with a high-resolution camera. The measurements were performed in a novel single-passage transonic wind tunnel to uncover the unsteady effectiveness of the endwall surface. Such effectiveness was dramatically influenced by the blowing ratios (*M*), showing attached flow at a low blowing ratio and lift-off at a high blowing ratio. The effectiveness was asymmetrically distributed due to the pressure gradients, jet compounding angle, and associated complex flows. The unsteady effectiveness was highly influenced by the energetic vortical structures, which interacted with the mainstream flow immediately behind the holes. It was featured by secondary structures (horseshoe, passage, and counter vortices) beside the JICF structures. Meanwhile, the unsteadiness was originated from the middle of the passage behind the holes. It is suggested to pay close attention to the locations of the holes for further optimization. This study could help the designers to understand the characteristics of unsteady effectiveness, promoting advanced cooling strategies for enhanced protection of future gas turbines.

## Introduction

Gas turbine is a heavy-duty engine that is used for many engineering applications, such as land-based power plants and civil/military aircraft, making the improvement of its output capacity of global concern. Based on the thermodynamic science [1], increasing the turbine thermal efficiency and corresponding gained power could be achieved at high turbine inlet temperature. Such temperature exceeds the melting point of the blade materials, leading to engine failure with its duty operations, which challenge the overall performance. Film cooling is one of the advanced cooling techniques that is used recently to protect the turbine blades from the incoming gases by introducing a secondary coolant flow over the hot surface, such as endwall region. However, it is known as a jet in crossflow phenomena (JICF), where the coolant penetrates the mainstream in a cross manner as discussed by Kelso et al. [2] and Andreopoulos and Rodi [3]. Once the coolant ejects from the holes, highly coolant and mainstream interactions happen immediately at the hole exit, producing a complex three-dimensional (3-D) vortical structure as discussed by Fric and Roshko [4] and Mahesh [5]. The vortical structures enforce the coolant to fluctuate over the protected surface (unsteady). Consequently, it could be completely or even partially

Content from this work may be used under the terms of the Creative Commons Attribution 3.0 licence. Any further distribution of this work must maintain attribution to the author(s) and the title of the work, journal citation and DOI.
Published under licence by IOP Publishing Ltd

exposed to hot gases, leading to local overheating. Such phenomena could thermally stress the turbine blades, leading to turbine failure with heavy-duty operations. Therefore, it is significantly desirable to understand the coolant unsteadiness (unsteady behaviour) behind turbine discrete holes.

In the past decades, a significant research work has been done for understanding of the physics behind the endwall film cooling, which was featured by highly complex flows. Such complexity was introduced by Langston et al. [6,7], who explored the detailed endwall structures. They captured interested structures accompanying the incoming flow boundary layers, which formed horseshoe vortex near leading-edge. These vortices are extended and developed as counter vortex near suction side (SS) and passage vortex near the pressure side (PS). These vortices interacted with the coolant flow from the discrete holes; leading to coolant deterioration and non-uniform distributions. Friedrichs et al. [8] visualized the interacting coolant and secondary flows and explained the local features of the hard cooling regions. Consequently, numerous efforts enhanced the coolant coverage over the endwall surface by optimized configurations. Friedrichs et al. [9] introduced an endwall configuration different from that of Friedrichs et al. [8], which revealed an improvement in the coolant spreading over the uncooled regions. Meanwhile, the optimized endwall configurations, which were introduced by Thole and Knost [10,11], achieved the desired enhancement, especially at the PS. Similarly, Li et al. [12,13] uncovered the endwall features and proposed optimized configurations to cool-down the hard cooling region at the leading-edge. Recently, Shiau et al. [14] proposed full-scale endwall configurations to improve the whole endwall surface, considering the upstream purge effects. The recent comparison of Shiau et al. [15] showed important features allied with the upstream injection angles through different configurations.

Although these studies successfully investigated the coolant behaviour behind the endwall configurations, they focused on the mean effectiveness; leaving a few unsteady studies. Kadotani and Goldstein [16] and Jumper et al. [17] examined the mainstream turbulence ($Tu$=0.3-20.6%) unsteadiness, which was found to decrease the effectiveness at low injection rates and increase it at high injection rates. In contrast, Mehendale et al. [18] and Du et al. [19] studied the upstream unsteady wakes, which showed palpable reductions in the effectiveness. Teng et al. [20] measured the mean and fluctuating thermal profiles within the holes influenced by upstream wakes, which were found to produce turbulence in the boundary layer profiles. The early study of Fawcett et al. [21] showed interesting unsteady coolant forms behind the discrete holes. They investigated the engine-representative film cooling unsteadiness on the mid-span of the blade PS, although the incoming flow Mach number was negligible. Their investigation was done behind at a wide range of coolant conditions using high-speed photography of particle image velocimetry measurement techniques. Their results revealed unsteady coherent shearing forms (structures) in the mainstream flow, which was strongly dependent on the coolant velocity. However, the unsteady JICF and complex flow unsteadiness over the endwall surface at transonic conditions have not been well understood yet.

This paper uncovered the unsteady endwall effectiveness at the engine-like conditions; aiming to capture the JICF and complex flow unsteadiness. High-resolution fast-PSP measurements are conducted over an endwall configuration at transonic condition using novel wind tunnel [22] (single-passage design). During the experiment, the coolant gas (i.e., $CO_2$, coolant to mainstream density ratio of $DR = \rho_c/\rho_\infty \approx 1.53$) is fed internally from a large plenum chamber through an upstream slot with blowing ratio of $M = DR(U_c/U_\infty)$=0.3 and row of cylindrical holes (located 20$D$ downstream) with blowing ratio of $M$=0.5-2.0. The measured effectiveness is analysed in terms of mean and unsteady quantities over the endwall surface. This paper is expected to deepen our understanding of the endwall unsteadiness.

## 1. Experiment setup and validation

### *1.1. High-speed test facility*

The current measurements are performed at transonic conditions using novel wind tunnel, which is designed by the author [22] as a single-passage at turbomachinery lab of Shanghai Jiao Tong University for film cooling studies. Figure (1a) shows the proposed design of the wind tunnel, which follows the

design of the high-duty inlet guide vane of Arts et al. [23] (i.e., Figure 1b). It consists of only single-passage that shaping the vane configuration through bounding the passage by two side walls. The design has two bleeds at the PS and SS to achieve the flow periodicity by removing the additional mainstream flows. This proposed strategy was firstly introduced by Blair [24] for simplified film cooling measurements. The design procedures of the proposed tunnel are achieved numerically before manufacturing via the periodic flow simulation and passage walls simulation. These procedures are performed on a high-duty inlet guide vane, which was tested by von Karman Institute [23] for isentropic Mach number of $M_{is}$=0.84. The proposed vane is shown in Figure (1b), which has a chord of 67.6 mm and pitch of 0.85 with axial flow inlet and 76° exit flow angle (see Arts et al. [23]). For consistency, the detailed procedures are found in Qenawy et al. [22].

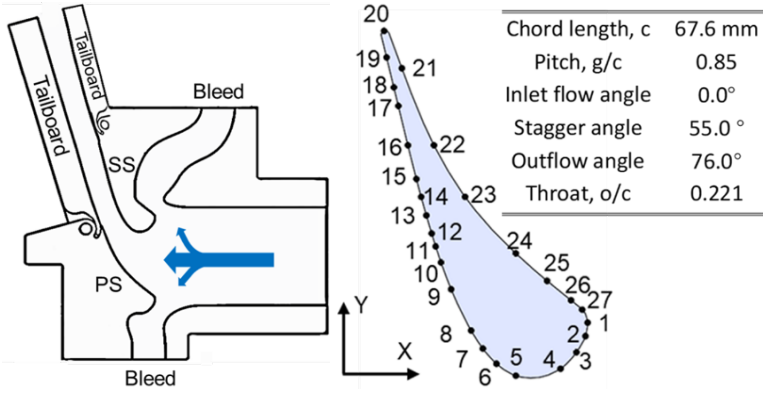


(a) Passage design (b) Passage shape

**Figure 1.** Novel single-passage transonic wind tunnel [22].

Figure (2a) shows the experiment setup of the current measurement. The mainstream flow is supplied into the wind tunnel by compressed air, being filtered to improve its quality. The desired flowrates, which are controlled using flow valve, are passed through big-chamber to reduce the acceleration and stabilize the flow before entering the passage. The air, then, is passed through three paths: two bleeds beside the passage. The majority of the air is flowed through the passage, while small amounts flow through the bleeds. The mainstream velocity is $U_\infty$=51.9 m/s as measured by a five-hole probe upstream of the passage. The turbulence intensity was $Tu$=2%, while the boundary layer thickness was $\delta$=3.1 mm as measured by (CTA-54T42, Denmark) hot wire anemometry. The suction bleed was observed by (SMC-PF3A706H, Japan) flowmeter, while the pressure bleed was observed by (SMC-PF3A703H, Japan) flowmeter, and both adjusted by flow control valves.

Figure (2b) shows the test model, which is installed underneath the passage with specific configurations. The model has a single-row of cylindrical holes with a hole diameter of $D$=1.0 mm (i.e., similar to engine conditions). The holes have 9$D$ entry length, 3$D$ spacing, and incline angle of 35° to the mainstream flow. Meanwhile, the model has a 1.5 mm slot width (located 20$D$ upstream of the holes). The model interior surface is carefully refined with 2000 sandpaper to ensure surface quality.

During the experiment, the coolant is discharged from a high-pressure $CO_2$ tank through a long pipeline and water bath to maintain the ambient temperature before feeding into the slot and discrete holes. The slot flowrate is observed by (FMA-1610A-OMEGA) flowmeter and maintained fix by adjusting the flow control valve at a blowing ratio of $M$=0.3. Similarly, the hole flowrates are monitored by (FMA-1610A OMEGA) flowmeter and adjusted by flow control valve with $M$=0.5-2.0. The coolant is fed from a plenum chamber to the endwall. The plenum is located underneath the test model and sealed to prevent coolant leakage. with a 1-mm-thick rubber gasket.

### *1.2. Film cooling measurement*

In film cooling, the coolant temperature ($T_c$) is relatively lower than the mainstream temperature ($T_\infty$), while the film temperature depends on the mixing conditions, which contribute the wall temperature. With insulated walls, the wall temperature is considered as adiabatic wall temperature ($T_{aw}$). Consequently, the adiabatic effectiveness ($\eta$) measures the efficiency of the coolant distributions over the surface. It is a non-dimensional temperature scale, which is defined by Eq. (1) [1,25].

$$\eta = \frac{T_\infty - T_{aw}}{T_\infty - T_c} \qquad (1)$$

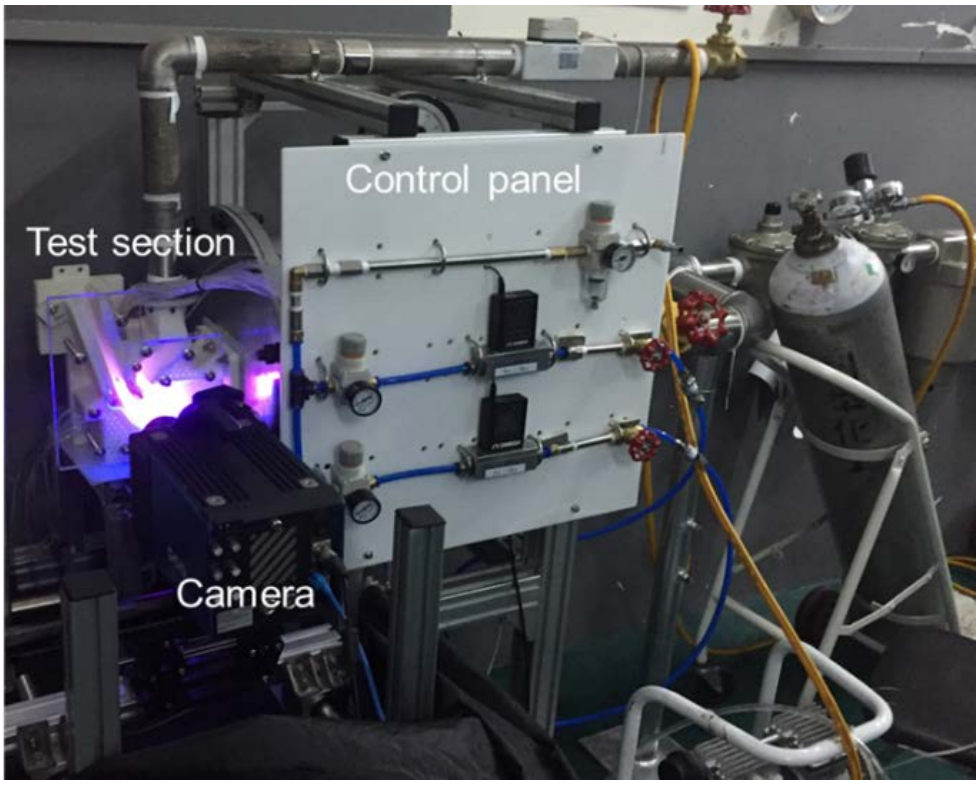


(a) Experimental setup

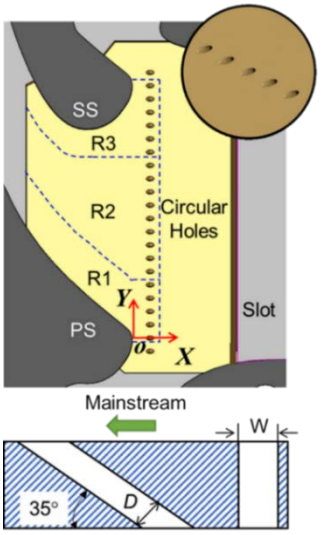


(b) Endwall configurations

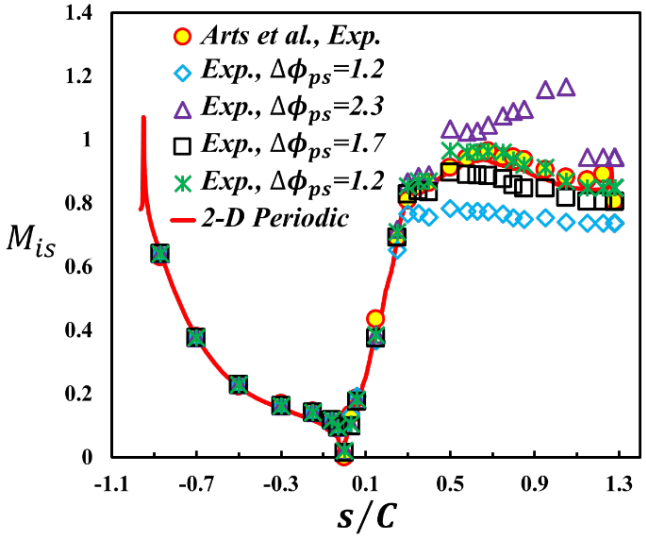


(c) Experimental validation

**Figure 2**. Current endwall measurement set up and validation.

In laboratories, heating the mainstream flow could increase the thermal losses through the walls, making the adiabatic conditions of hard lab achievement. Recently, the measurement is performed in isothermal conditions, using heat and mass transfer analogy. Theoretically, analogy of heat and mass transfer could be considered; if the concentration and thermal boundary layers are of the same order, which means unity of Lewis number (i.e., $Le = \alpha_s/D_s \approx 1.0$, where $D_s$ is the concentration diffusion coefficient and $\alpha_s$ is the thermal diffusion). By making the coolant and mainstream flow different gases with the same temperatures (isothermal), the main focus will be the oxygen concentration. Consequently, the effectiveness (Eq. 1) can be expressed by Eq. (2) as reported by Charbonnier et al. [26]; where $W_c/W_\infty$ is the coolant to mainstream molecular weight ratio and $P_{O2,\infty}/P_{O2,mix}$ is the partial oxygen pressure.

$$\eta = 1 - \frac{1}{\left[\left(\frac{P_{O2,\infty}}{P_{O2,mix}}\right)_{aw} - 1\right]\frac{W_c}{W_\infty} + 1} \qquad (2)$$

Pressure sensitive paint (PSP), based on the mass transfer analogy ($Le \approx 1$), is quite a new kind of non-contact optical method for pressure measurement. It has been widely used to simulate the heat transfer process due to its ability to run in isothermal conditions, where heat conduction problems could be eliminated. Meanwhile, it is a reliable technique, which is based on the measurement of Wright et al. [27] and can verify the coolant effectiveness under adiabatic conditions. Besides, PSP can provide detailed coolant separations, lift-off, and reattachment phenomena. For example, Johnson et al. [28] captured a good agreement of PSP measurement in comparison with the open literature. Interestingly, our recent publications [29–34] showed an acceptable agreement of PSP immediately at the hole exit.

The present paint is a mixture of luminescent molecules, silicon dioxide particles, and polystyrene (binder). This study is performed using fast-response particle pressure-sensitive paint (fast-PSP) to resolve the dynamics of the fluctuating effectiveness. The silicon dioxide particles have a hollow and porous structure, leading to fast responding to the pressure fluctuations. It was developed and improved by Peng et al. [35]. It is prepared in-house with dynamic response of ~9.5 kHz (corresponding response time of ~106 μs) [35] on the shock tube. It is resolved by dichloromethane mixture, spread over the test surface by airbrushes, and kept in insulated/cleaned conditions for ~5 hours to dry.

In theory, PSP emits luminescence when exposed to an appropriate wavelength. However, the emitted intensity is influenced by the oxygen partial pressure, which is known as the oxygen quenching. Through it, especially via reduced emission in the presence of oxygen, excited molecules could be returned into their ground states. It could be caused by the quenching of some luminophores through the collision with the oxygen molecules. So, the intensity of the photo-luminescence is proportional inversely to the local oxygen concentration. Therefore, the emitted intensity decreases with increasing the oxygen partial pressures, which can be evaluated through the Stern–Volmer relationship [29,30], obtained by the calibration procedures. In contrast, the emitted intensity is captured by a CCD camera, which has a 650±25 nm filter to remove the background noise after exiting the paint by 385 nm UV light. During the experiment, the atmospheric air simulates the incoming hot gases in the real engine, while the oxygen-free foreign gas (e.g., CO2) is used as a coolant.

In this study, the endwall model is painted with black primer to reduce both transmission and reflection. Fast-PSP, which is used to measure the mean and unsteady effectiveness, is sprayed with an airbrush in an isolated condition and kept ~5 hours to dry. An ultraviolet LED (LM2X-DM, ISSI) as an excitation source was used with 385 nm wavelength. A complementary metal-oxide-semiconductor camera (PCO, HS4, high-speed) at a sampling rate of 10 Hz was used to record the photoluminescence light emission. A 650±25 nm wavelength band-pass filter is fixed ahead of the camera to filter the background noises.

### *1.3. Uncertainty analysis*

In this study, the uncertainty arises from two main sources; measurement as well as device/instrument uncertainties. In the wind tunnel and test models, the uncertainty originally comes from the 3-D printer with a printing accuracy of ±1% and approximate resolution of ~50 μm based on manufacturing details. For measurement, the uncertainties in the instruments are taken from the supplier as:

- The uncertainty of the incoming flow pressure reading is ±2%, while temperature reading is ±2%.
- The uncertainty of the 5-probes pitot tube is ± 2%.
- The uncertainty of the SMC flowmeters is ±2%, while of OMEGA flowmeters is ±1%.
- The uncertainty of the pressure transducer is ± 1%.
- The uncertainty of the blowing ratios is ±2.6%, while of the measured $M_{is}$ is ±2.8%.

For the PSP measurement, to minimize uncertainties, an interrogation window of 5 x 5 pixels and 50% overlapping are applied on the spatially-averaged procedures. The image resolution was ~0.06 mm/pixel (corresponding spatial resolution of ~0.1*D*). Based on the estimation of Johnson & Hu [36], the uncertainty of PSP measurement is 8% near the hole (high effectiveness regions) and 12% downstream (low effectiveness regions), which is probably related to mainstream and coolant conditions, PSP calibration procedures, and quality of the captured image. However, the accelerated mainstream (compressibility effects) increases the uncertainty of the measured effectiveness; resulting in 10% near the hole and 15% downstream.

*1.4. Measurement validation*

Figure (2c) shows the distributions of the isentropic Mach number ($M_{is}$) on the mid-span of the passage height in comparison with Arts et al. [23] and the periodic simulation. Notably, $M_{is}$ was computed in Eq. (3) based on the local static pressure (*P*) of the distributed pressure taps along with the vane SS and PS (see Figure 1b), where $P_0$ is the stagnation pressure at the passage leading-edge and $\gamma$ is the heat capacity ratio. By adjusting the tailboard angle, the results provide a good agreement with PS adjustable angle of $\Delta\Phi_{ps}$=2.0°, which denotes the validation of the current study.

$$M_{is} = \sqrt{\frac{2}{\gamma - 1}\left(\left(\frac{P_0}{P}\right)^{\frac{\gamma-1}{\gamma}} - 1\right)} \qquad (3)$$

*1.5. Time-average and statistical effectiveness*

The measured instantaneous film cooling effectiveness (i.e., Eq. 2) is analysed into mean (i.e., $\bar{\eta}$) and fluctuating (i.e., $\acute{\eta}$) components (i.e., $\eta = \bar{\eta} \pm \acute{\eta}$). The mean effectiveness is calculated by averaging the captured instantaneous snapshots via Eq. (4).

$$\bar{\eta} = (1/t)\int_0^t \eta \, dt \qquad (4)$$

Meanwhile, the standard deviation (*SD*) is used to measure the variation of the data from the mean value. In statistical science, low *SD* means low fluctuations (close to the mean value), while high *SD* indicates high fluctuations (far from the mean value). As the measured effectiveness has large instantaneous data-sets, it would be useful to evaluate its fluctuations from the mean value. Therefore, *SD* is defined by Eq. (5); where *N* is the number of instantaneous snapshots.

$$SD = \sqrt{\frac{1}{N-1}\sum_{i=1}^{N}(\eta_i - \bar{\eta})^2} \qquad (5)$$

Figures (3-4) show the time-average and statistical distributions of the measured effectiveness over the endwall surface at *M*=0.5, 1.0, 1.5, and 2.0. For all figures, the coolant from the upstream slot exhibits almost the same footprints. It has accumulated through the passage's middle, flowing toward the SS,

forming asymmetrical distributions. Such accelerated flow, as reported in Du and Li [37], could drive more coolant toward the passage vortex line, under the effects of pressure gradient [6,7]. Immediately, the coolant is widely spread behind the exit of the slot and develops narrower downstream before merge with the coolant flow from the holes, which agree with Chen et al. [38,39]; revealing the contribution of the upstream slot to the endwall coolant effectiveness. On the other hand, the corresponding *SD* of the measured effectiveness behind the holes is quite similar to the mean effectiveness. Noticeably, the *SD* signatures are influenced by both JICF and complex flows, where high effectiveness regions have low *SD* values; indicating inverse proportional to the mean distributions. However, the unsteady analysis is performed only behind the holes for a better understanding of the JICF and complex flow unsteadiness.

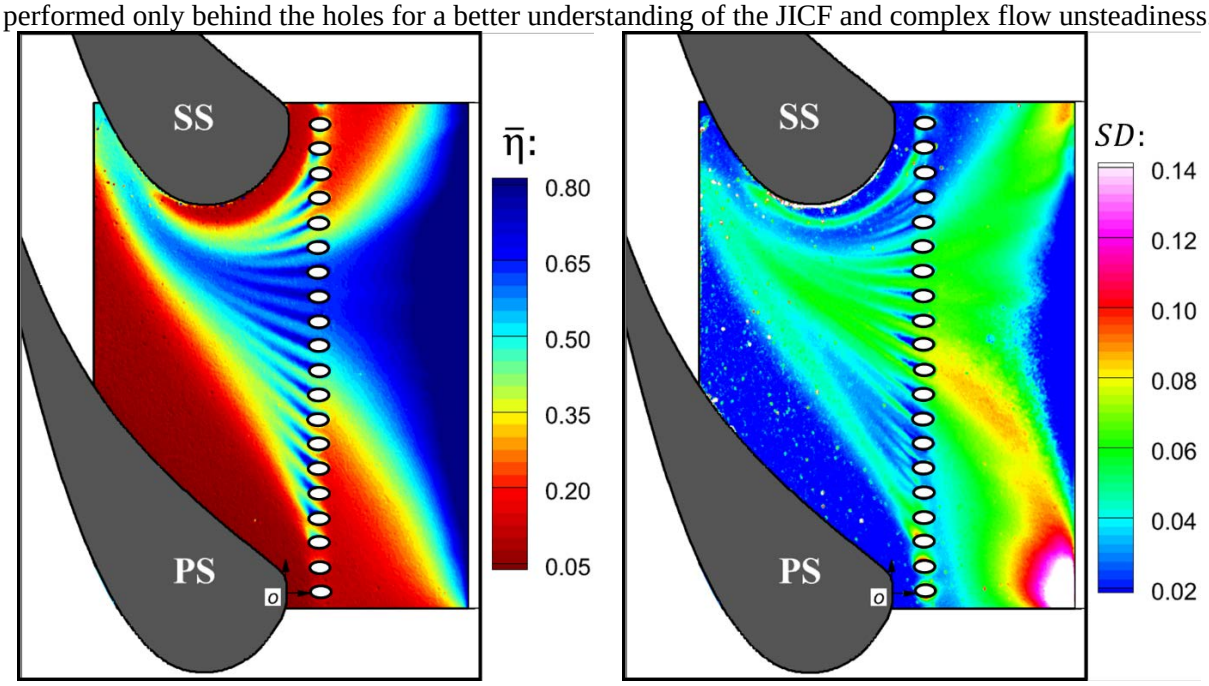


(a) *M*=0.5

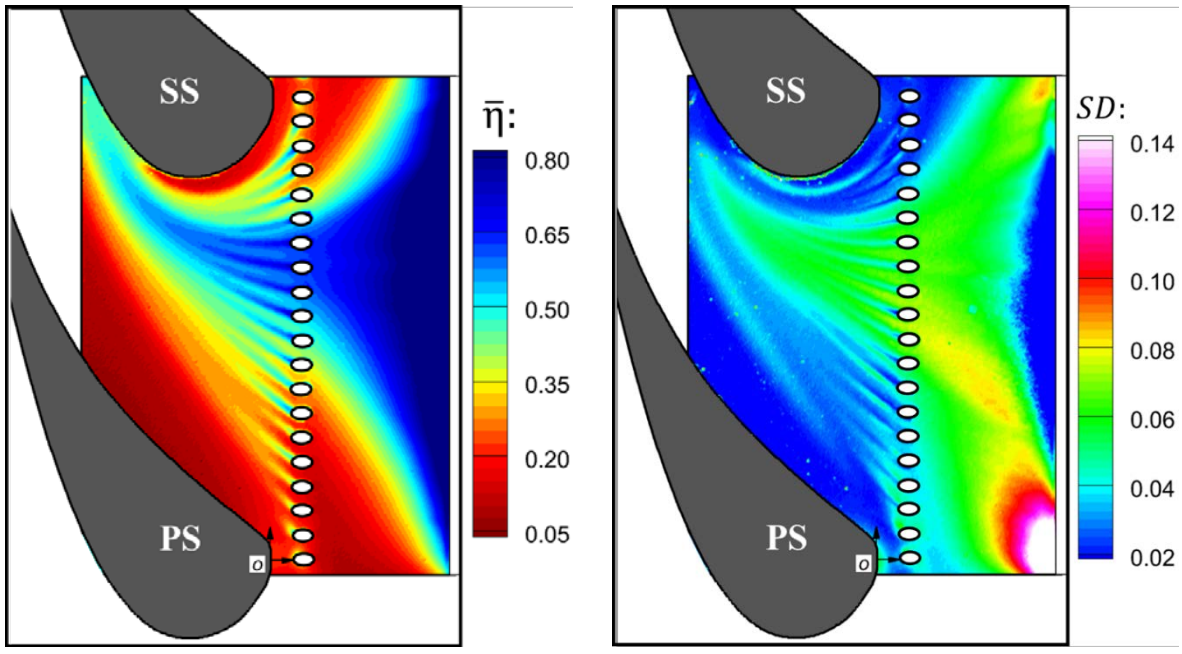


(b) *M*=1.0

Figure 3. Endwall film cooling distribution at blowing ratio of M=0.5 and 1.0; (left) Time-average and (right) Standard deviation.

For *M*=0.5 (Figure 3a), the coolant asymmetrically spreads over the endwall, concentrating on the SS, where the passage vortex propagates [6,7]. The passage vortices at the PS force the coolant movement toward SS. Consequently, SS exhibits higher effectiveness due to the coolant merging from the holes and slot, while the PS, especially the downstream region is relatively uncooled. In contrast, at leading-edge, less coolant has observed, where the horseshoe vortices dominate the flow region, leading to blows coolant away, Friedrichs et al. [8,9]. Carefully examining the leading-edge at SS, rarely coolant is observed at the endwall junction indicating that the horseshoe vortex sweeps the coolant into the mainstream flow. Interestingly, no injection can be discharged through the PS holes (i.e., last two holes). Sundaram and Thole [40,41] reported a quite similar phenomenon, which was originated from low coolant momentums, leading to incapability of ejection through those holes. On other hand, the contour shows high *SD* values upstream the SS from the 2$^{nd}$ and 3$^{rd}$ holes. This *SD* signature probably originates from the horseshoe vortex (leading-edge) and associates with downstream counter vortex. Meanwhile, the contour shows high *SD* values near the PS from the 3$^{rd}$ and 4$^{th}$ holes; associated with the passage acceleration streamlines. Plausibly, the coolant accumulates along the passage vortex line and be highly unsteady downstream. In contrast, the middle region shows high *SD* values at the centre, which associates with the downstream counter-rotating vortex-pair (CRVP) and single-asymmetric main-vortex (SAMV) structures, as proposed by Li et al. [42]. Meanwhile, the lateral sides show low *SD* values; due to less coolant at the PS and due to the coolant accumulation at the SS.

For *M*=1.0 (Figure 3b), coolant is widely spread behind the holes across the endwall (the aforementioned converging coolant trace becomes much wider and more uniform). Due to enough coolant momentums, the coolant overcomes the mainstream flow, leading to obvious coolant distributions at the passage PS. The coolant partially lifts the endwall off in the near-holes region and diverts broadly downstream. On the other hand, the *SD* signatures are quite insignificant compared with *M*=0.5 due to the coolant partially lifts-off the surface. The unsteady horseshoe and corresponding counter vortices have weak *SD* signatures at the passage SS. Similarly, the passage acceleration line has weak *SD* signatures at the PS. Plausibly, this absence of the *SD* signatures is caused by insufficient coolant attachments to the endwall surface. In contrast, the passage middle shows apparent *SD* signatures associated with the coolant structures (i.e., CRVP and SAMV). Plausibly, the attached flow propagates along the passage acceleration lines; making the coolant highly unsteady downstream.

For *M*=1.5 (Figure 4a), the coolant footprints exhibit dissimilar events. The middle region, which characterizes highly accumulated flow, shows a slight reduction in the coolant effectiveness compared with *M*=1.0. The increased momentum of coolant jets can overcome the negative pressure within the passage. Obviously, the visible trace behind the holes shows coolant lift-off phenomena near PS. Interestingly, increasing coolant momentums behind the holes improves the effectiveness of the vane leading-edge. Although the coolant lifts the endwall surface, it interacts with the leading-edge vortices (i.e., horseshoe). The horseshoe vortex forces the coolant to flow downward and impinge onto the endwall leading-edge. On the other hand, the *SD* contour at *M*=1.5 exhibits almost similar behaviour as *M*=1.0 behind the holes. The coolant unsteadiness decreases at the PS and SS, while increases at the passage middle. Plausibly, the coolant is completely lift-off the endwall surface near the PS and SS with the unsteady accumulated flow at the passage middle. However, the passage leading-edge shows *SD* signatures at either PS or SS, which are caused by the unsteady reattached flow.

For *M*=2.0 (Figure 4b), the coolant has highest momentums. The coolant jets near the PS shows obvious separation from the endwall surface, observing from the effectiveness reductions in the contours. However, the hard to cool [11] region (i.e., near the leading-edge) has been pointedly enhanced by the coolant flow, indicating rebus coolant behaviours. On the other hand, the attached flow becomes more unsteady for *M*=2.0 compared with the aforementioned blowing ratios. The passage middle region shows highly unsteady *SD* signatures, which is probably caused by the unsteady accumulated flows. Meanwhile, the leading-edge shows clear signature of the horseshoe vortex from such a reattached flow

at both PS and SS. In contrast, the *SD* signature at the PS extends little downstream, which could associate with the passage vortex interactions with the reattached flow.

*1.6. Fluctuating Effectiveness*

To fully understand the measured standard deviation, the fluctuating effectiveness (i.e., $\acute{\eta}$) through the interval time is presented in Figures (5-6). For consistency, only the fluctuating component at *x/D*=0.0 and 3.0 behind the holes is presented. Generally, the coolant and mainstream flows are in sparring; as indicated by blue and red colour maps over the endwall surface.

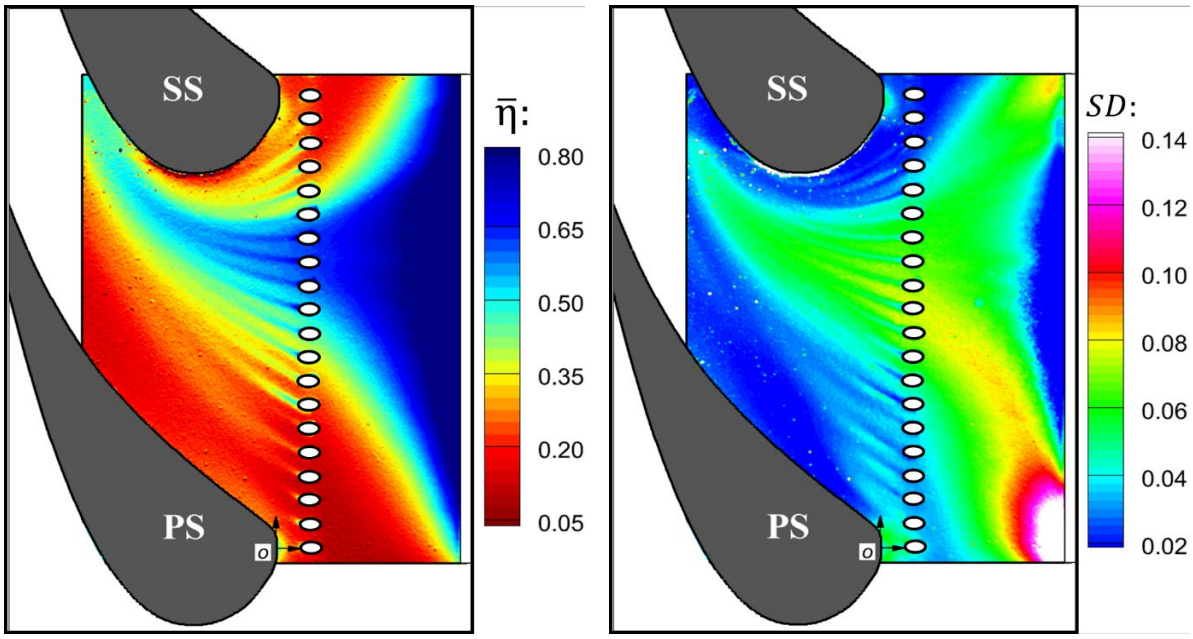


(a) *M*=1.5

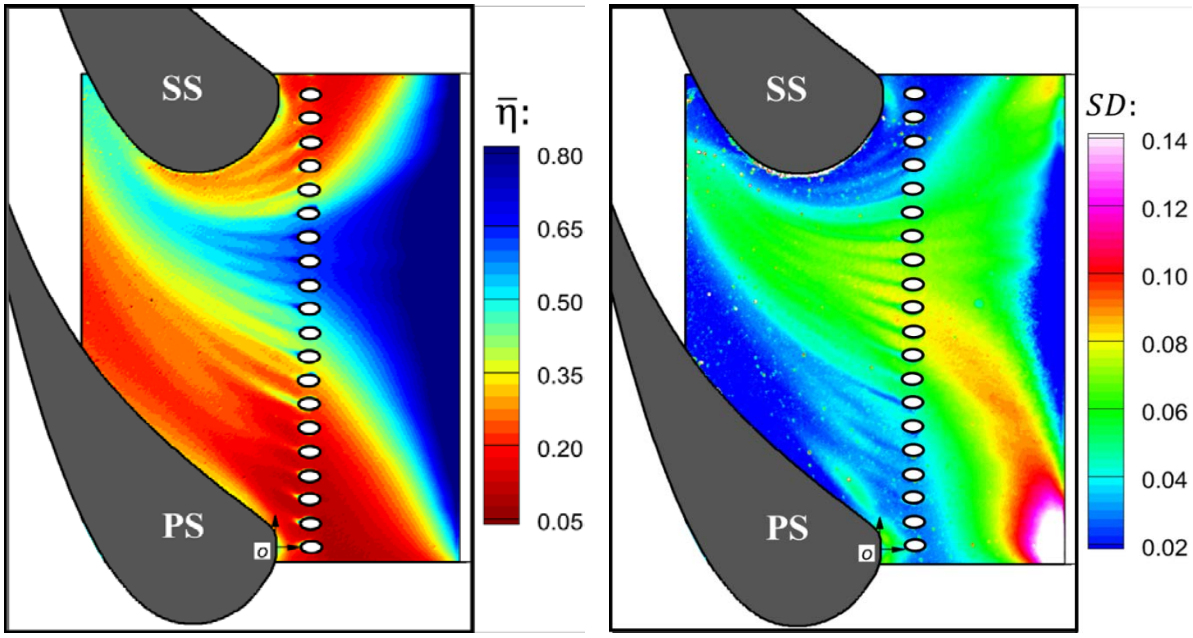


(b) *M*=2.0

**Figure 4.** Endwall film cooling distribution at blowing ratio of *M*=1.5 and 2.0; (left) Time-average and (right) Standard deviation.

Figure (5) shows the instantaneous fluctuating effectiveness downstream of the holes (i.e., *x/D*=0.0 and 3.0) at low blowing ratio (i.e., *M*=0.5 and 1.0). For *M*=0.5, the contours show obvious sparring between coolant and mainstream flows. The major fluctuations originate in the middle of the passage (i.e., close to the SS), which is consistent with the *SD* distributions (Figure 3a). Near the SS, there is a column of fluctuating effectiveness immediately at the hole exit (i.e., *x/D*=0.0) near *z/D*≈50, which is caused by the passage horseshoe vortex. Meanwhile, this fluctuating column slightly moves toward the middle of the passage (i.e., *z/D*≈47) at 3D downstream of the hole exit (i.e., *x/D*=3.0); leaving a blank column at *z/D*≈51. Plausibly, the passage horseshoe vortex becomes a downstream counter vortex. In contrast, there is another column of fluctuating effectiveness immediately at the hole exit (i.e., *x/D*=0.0) near the PS (i.e., *z/D*≈11), which associates with the passage acceleration line. This is observed from the inward orientation of the passage acceleration downstream (i.e., *x/D*=3.0), which originates at *z/D*≈17. For *M*=1.0, the major fluctuations originate in the passage's middle near SS. This agrees with *SD* distributions (Figure 3b); revealing unsteady accumulation flow. Interestingly, no pure signature exists for either passage horseshoe/counter vortices at the SS or acceleration flow at the PS; revealing coolant lift-off. Generally, the cylindrical holes exhibit higher fluctuations in the middle of the passage.

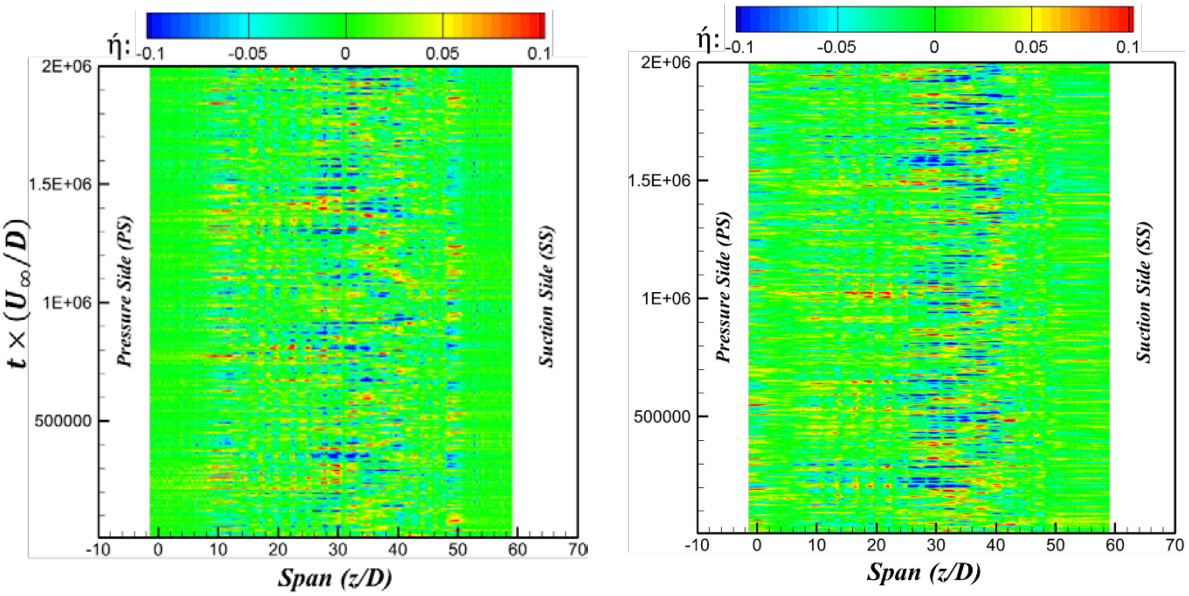


(a) Immediately at the hole exit *x/D*=0.0

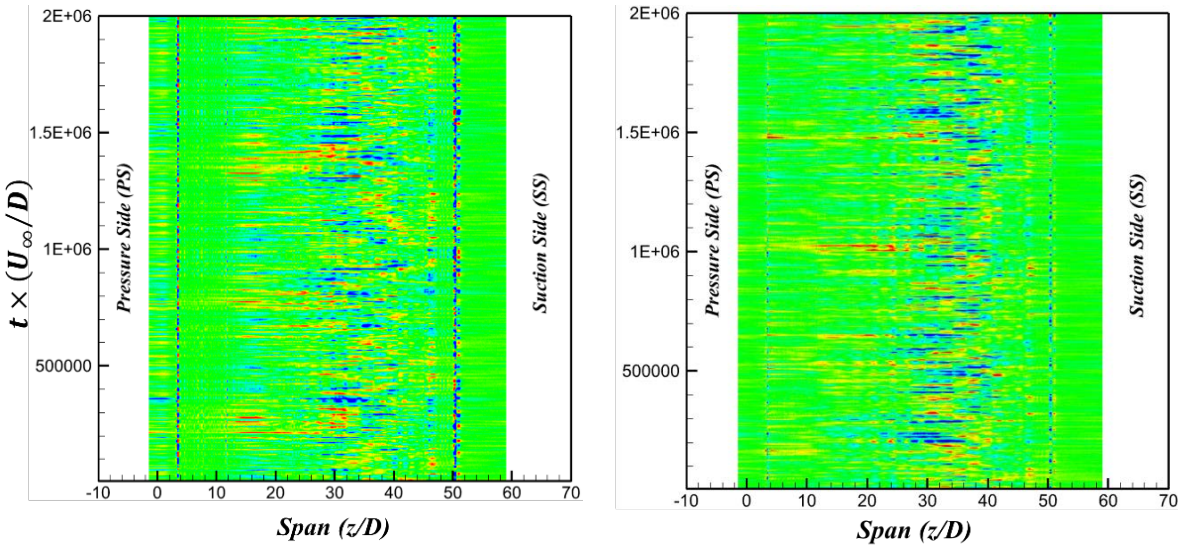


(b) 3*D* downstream of the hole exit (*x/D*=3.0)

**Figure 5.** Fluctuating effectiveness at (left) *M*=0.5 and (right) *M*=1.0.

Figure (6) shows the fluctuations of the measured effectiveness downstream of the discrete holes (i.e., *x/D*=0.0 and 3.0) at high blowing ratio (i.e., *M*=1.5 and 2.0). For *M*=1.5, the fluctuations still originate in the middle of the passage near the passage SS; revealing the unsteady coolant flow from the upstream slot. Interestingly, the passage horseshoe vortex is observed immediately at the hole exit (i.e., *x/D*=0.0) at *z/D*≈56 and *z/D*≈0.0 near the SS and PS, respectively. Plausibly, the reattached coolant flow near the leading-edge mixes with such horseshoe vortices; revealing unsteady effectiveness and explaining the *SD* signatures at the passage leading-edge in Figure (4a). Generally, the cylindrical holes still exhibit higher fluctuations near passage's middle compared with PS and SS. For *M*=2.0, the fluctuations increase at the middle, which reveal obvious unsteady coolant from the upstream slot. The reattached passage horseshoe vortex originates at *x/D*=0.0 near both SS (*z/D*≈58) and PS (*z/D*≈0.0). Meanwhile, the downstream behaviour (i.e., *x/D*=3.0) shows a weak signature near the PS, which originates from the reattached flow (see mean effectiveness distributions in Figure 4b).

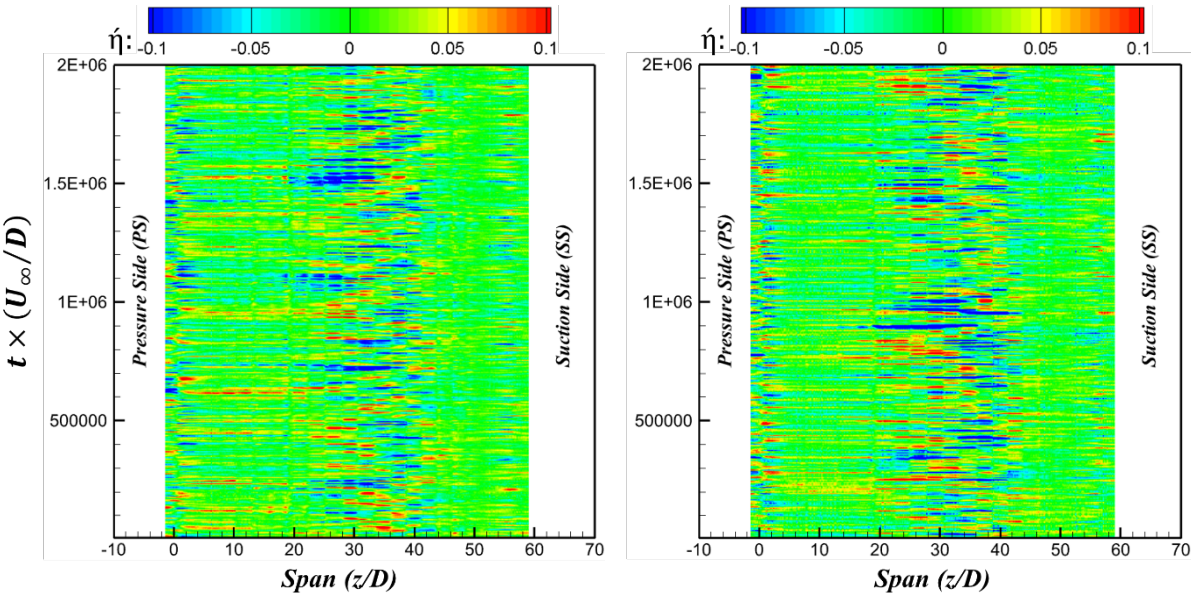


(a) Immediately at the hole exit (*x/D*=0.0)

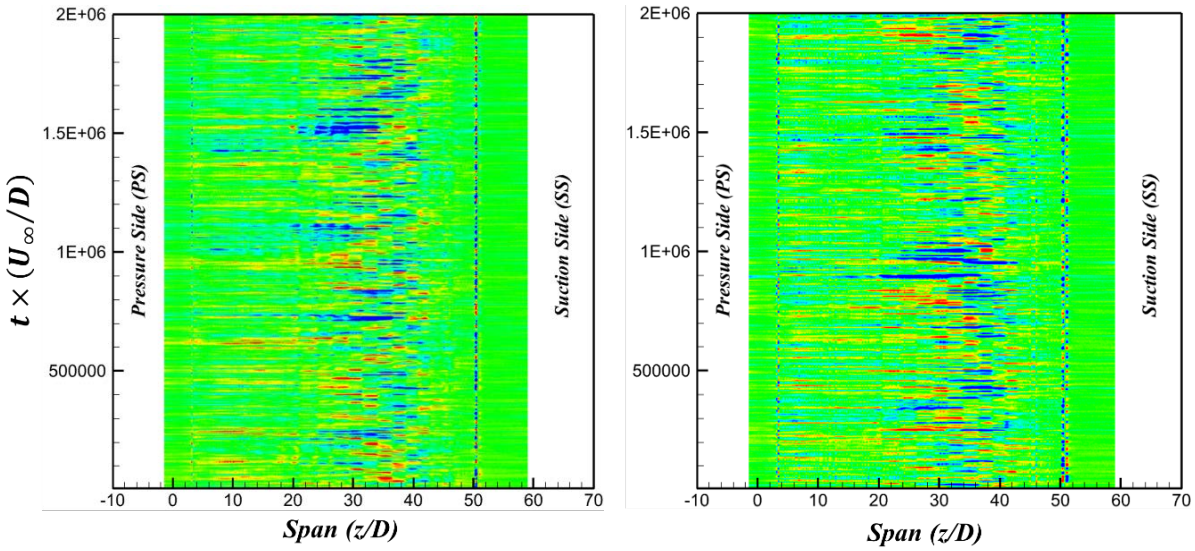


(b) 3*D* downstream of the hole exit (*x/D*=3.0)

**Figure 6.** Fluctuating effectiveness at (left) *M*=1.5 and (right) *M*=2.0.

## 2. Conclusion

In this contribution, unsteady endwall effectiveness behind the discrete holes was measured, considering the JICF and complex flow effects. The measurements were performed in a novel single-passage transonic wind-tunnel at $M_{is}$=0.84; showing acceptable agreements with literature's available data. High-resolution fast-PSP measurements were conducted to uncover the endwall unsteady effectiveness. Coolant gas ($CO_2$, *DR*≈1.53) fed into the endwall model with slot and row of holes (*M*=0.3 for slot and *M*=0.5-2.0 for holes). Generally, endwall exhibited an asymmetrical effectiveness distribution, featuring higher effectiveness near the SS, following by middle region, and lower near PS. The passage vortices as well as flow structures at SS was responsible for cooling spreads, which was found to be stronger behind the holes, leading to decline endwall coverage. Due to pressure gradient, the coolant is enforced toward SS, resulting in higher cooling effectiveness. The unsteady analysis over the endwall surface revealed the contributions of large-scale structures to the unsteady effectiveness. In addition, the *SD* signatures were associated with the endwall passage, counter, and horseshoe vortices besides the CRVP and SAMV structures. The unsteadiness originated from the coolant accumulations in the middle of the passage along the coolant acceleration lines. While the current work focuses on the endwall unsteadiness, still additional investigation with various design configurations is required for increasing the coolant coverages with special considerations of local flow features.

## Acknowledgments

The authors thankfully acknowledge the financial support of the current work from National Natural Science Foundation of China (51806138, 11725209).

## Nomenclature

| | |
|---|---|
| $D$ | Hole diameter |
| $DR$ | Density ratio |
| $M$ | Blowing ratio |
| $M_{is}$ | Isentropic Mach number |
| $P$ | Static pressure |
| $P_o$ | Total pressure |
| $\frac{P_{o2,\infty}}{P_{o2,\mathrm{mix}}}$ | Oxygen partial pressure |

| | |
|---|---|
| $T_c$ | Coolant temperature |
| $T_\infty$ | Mainstream temperature |
| $T_{aw}$ | Adiabatic wall temperature |
| $W$ | Width |
| $\frac{W_c}{W_\infty}$ | Molecular weight ratio |
| $x, y, z$ | Cartesian coordinates |

Greek symbols

| | |
|---|---|
| $\eta$ | Instantaneous effectiveness |
| $\bar{\eta}$ | Mean (time-average) effectiveness |
| $\acute{\eta}$ | Fluctuating effectiveness |
| $\Delta\emptyset_{ps}$ | PS deviation angle |

Abbreviations

| | |
|---|---|
| CRVP | Counter-Rotating Vortex-Pairs |
| Fast-PSP | Fast Pressure-Sensitive Paint |
| JICF | Jet in Cross Flow |
| PS | Pressure Side |
| SD | Standard Deviation |
| SS | Suction Side |
| SAMV | Single-Asymmetric Main-Vortex |

## References

[1] Han J C and Rallabandi A P 2010 *Front. Heat Mass Transf.* **1** 1-21.
[2] Kelso R M, Lim T T and Perry A E 1996 *J. Fluid Mech.* **306** 111-144.
[3] Andreopoulos J and Rodi W 1984 *J. Fluid Mech.* **138** 93-127.
[4] Fric T F and Roshko A 1994 *J. Fluid Mech.* **279** 1-47.
[5] Mahesh K 2011 A*nnu. Rev.* Fluid *Mech.* **45** 379-407.
[6] Langston L S, Nice M L and Hooper R M 1977 *J. Turbomach*. **99** 21-28.
[7] Langston L S 1980 *J. Eng.* Gas *Turbines Power* **102** 866-874.
[8] Friedrichs S, Hodson H P and Dawes W N 1995 *Proc. ASME Turbo-Expo* Paper No. 95-GT-001.
[9] Friedrichs S, Hodson H P and Dawes W N 1999 *J. Turbomach.* **121** 772-780.
[10] Thole K A and Knost D G 2005 *Int. J. Heat Mass Transf.* **48** 5255-5269.
[11] Knost D G and Thole K A 2005 *J. Turbomach.* **127** 297-305.
[12] Li X, Ren J and Jiang H 2015 *Int. J. Heat Mass Transf.* **90** 1-14.
[13] Li X, Ren J and Jiang H 2016 *Int. J. Heat Mass Transf.* **102** 348-359.
[14] Shiau C C, Chen A F, Han J C, Azad S and Lee C P 2016 *J. Turbomach* **138** 051002.
[15] Shiau C C, Sahin I, Wang N, Han J C, Xu H and Fox M 2019 *J. Therm. Sci. Eng. Appl.* **11** 031012.
[16] Kadotani K and Goldstein R J 1979 *J. Eng. Gas Turbines Power* **101** 459-465.
[17] Jumper G W, Elrod W C and Rivir R B 1991 *J. Turbomach.* **113** 479-483.
[18] Menhendale A B, Han J C, Ou S and Lee C P 1994 *J. Turbomach.* **116** 730-737.
[19] Du H, Han J C and Ekkad S V 1998 *J. Turbomach.* **120** 808-817.
[20] Teng S, Sohn D K and Han J C 2000 *J. Turbomach.* **122** 340-347.
[21] Fawcett R J, Wheeler A P S He L and Taylor R 2012 *J. Turbomach.* **134** 021015.
[22] Qenawy M, Yuan L, Liu Y, Peng D, Wen X and Zhou W 2020 *J. Eng. Gas Turbines Power* **142** 071009.
[23] Arts T, Rouvroit M L D and Rutherford A W 1990 Von Karman Institute Report No. 174.
[24] Blair M F 1974 *Proc. ASME Turbo-Expo* Paper No. 74-GT-33.
[25] Bogard D G and Thole K A 2006 *J. Propuls. Power* **22** 249-270.
[26] Charbonnier D, Ott P, Jonsson M, Cottier F and Köbke T 2010 *Proc. ASME Turbo-Expo* Paper No. GT2009-60306.
[27] Wright L M, Gao Z, Varvel T A and Han J C 2009 *Proc. ASME Turbo-Expo* Paper No. HT2005-

72363.
[28] Johnson B, Tian W, Zhang K and Hu H 2014 *Int. J. Heat Mass Transf.* **76** 337-349.
[29] Khojasteh A R, Wang S F, Peng D, Yavuzkurt S and Liu Y 2017 *Int. J. Heat Mass Transf.* **110** 629-642.
[30] Cai T, Peng D, Yavuzkurt S and Liu Y Z 2018 *Int. J. Heat Mass Transf.* **120** 1325-1340.
[31] Zhou W, Peng D, Liu Y and Hu H 2019 *Exp. Therm. Fluid Sci.* **101** 16-26.
[32] Qenawy M, Chen H, Peng D, Liu Y and Zhou W 2020 *J. Turbomach.* **142** 041007.
[33] Zhou W, Qenawy M, Liu Y, Wen X and Peng D 2019 *Int. J. Heat Mass Transf.* **129** 569-579.
[34] Zhou W, Chen H, Liu Y, Wen X and Peng D 2018 *Phys. Fluids* **30** 127103.
[35] Peng D, Gu F, Li Y and Liu Y 2018 *Sensors Actuators, A Phys.* **279** 390-398.
[36] Johnson B and Hu H 2016 *J. Turbomach.* **138** 121004.
[37] Du K and Li J 2016 *Int. J. Heat Mass Transf.* **98** 768-777.
[38] Chen P, Alqefl M, Li X, Ren J, Jiang H and Simon T 2019 *Int. J. Therm. Sci.* **142** 233-246.
[39] Chen P, Li X, Ren J, Jiang H and Simon T 2019 *Int. J. Heat Mass Transf.* **137** 690-702.
[40] Sundaram N and Thole K A 2008 *J. Turbomach.* **130** 041013.
[41] Sundaram N and Thole K A 2009 *J. Turbomach.* **131** 041007.
[42] Li W, Li X, Ren J and Jiang H 2017 *Int. J. Therm. Sci.* **121** 410-423.